Intermetallics 163 (2023) 108074

Contents lists available at ScienceDirect

Intermetallics

journal homepage: www.elsevier.com/locate/intermet

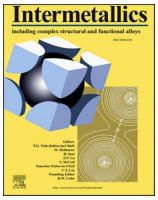

Influence of Mo and B additions in intermetallic near-Fe_3Al alloys on microstructure and mechanical properties

Andreas Abel [a,*], Julian M. Rosalie [a], Stefan Reinsch [a], Pawel Zapala [b], Heiner Michels [b], Birgit Skrotzki [a]

[a] Federal Institute for Materials Research and Testing (BAM), Department of Materials Engineering, 12205, Berlin, Germany
[b] Access e.V., Intzestr. 5, 52072, Aachen, Germany

ARTICLE INFO

Keywords:
A. aluminides
B. alloy design
B. mechanical properties
B. solid-solution hardening
C. casting
D. microstructure

ABSTRACT

Iron aluminides, already reported in the late 19th century, did not cease to attract the interest of scientists and engineers ever since. Besides good oxidation resistance, low density and resource availability, potentials for high-temperature strengths that compete with high-alloy steels were unlocked by low alloy contents. Still, research on alloy design continues, as alloying usually comes at the price of brittleness in low-temperature regimes. A potential candidate is the quinary Fe–Al–Mo–Ti–B system which is strengthened by solid solution and eutectic borides. It was shown to have good strength and outstanding creep resistance under compressive loading up to elevated temperatures. Although the individual effect of alloy additions is well understood in iron aluminides, little is known about the combined effects of alloying concentrations on microstructure, phase stability and mechanical properties. Therefore a systematic study of two Ti-doped near-Fe_3Al alloys with varying contents of Mo (2–4 at.%) and B (0.5–1 at.%) was conducted. In total eight different alloys were fabricated by investment casting into ceramic shell molds. Alloys were characterized and compared by grain size, phase transitions, microstructure evolution as well as elemental compositions and volume fractions of phases. For mechanical characterization, macrohardness and microhardness tests as well as tensile tests at ambient and high temperatures were conducted. Independent of alloy additions, alloys with 24–25 at.% Al exhibit superior proof strength due to a higher matrix hardness. Decreasing B content generally decreases strength by lower secondary phase fractions which contribute via particle hardening. Reducing Mo content decreases both the solute concentration in the matrix and secondary phase fractions. Surprisingly, strength is similar or even superior to alloys with higher Mo content. Strength relations are discussed with a focus on solid-solution hardening theory and other competing strengthening mechanisms.

1. Introduction

Iron aluminides are subject to a lasting interest due to their good specific strength, outstanding oxidation resistance and good availability of raw materials. Thus Fe–Al alloys are potential candidates for structural applications in hot and corrosive environments [1–4]. Processing of Fe–Al was successfully demonstrated in standard techniques such as casting, forging, rolling, powder metallurgy and additive manufacturing [5–8]. The manufacture of complex parts often requires casting strategies such as investment casting and centrifugal casting which was already demonstrated on an industrial scale for Fe-Al [5,9]. Still, only a few applications have been realized so far [1,2,10–12]. The two main reasons are that ductility at ambient temperatures is usually low [13] and strength at temperatures above 600 °C is not sufficient to replace conventional high-temperature materials [14]. Therefore, research mostly focussed on alloying concepts to improve high-temperature strength [9,15–17]. At the same time, attention is paid to not compromising ductility as alloying usually shifts the brittle-to-ductile transition temperature (BDTT) to higher temperatures [18]. The development of new promising alloying systems and the demand for more sustainable, but heat-resistant and economical materials currently stimulate undertakings for re-evaluating applications in the energy, automotive, naval and aeronautical sectors [18]. One new candidate is the Fe_3Al–Mo–Ti–B system of which a few compositions have been already

* Corresponding author.
E-mail addresses: andreas.abel@bam.de (A. Abel), julian.rosalie@bam.de (J.M. Rosalie), stefan.reinsch@bam.de (S. Reinsch), p.zapala@access-technology.de (P. Zapala), h.michels@access-technology.de (H. Michels), birgit.skrotzki@bam.de (B. Skrotzki).

https://doi.org/10.1016/j.intermet.2023.108074
Received 1 August 2023; Received in revised form 21 September 2023; Accepted 24 September 2023
Available online 8 October 2023

studied [4,19,20]. Within the $D0_3$-stabilized region of the Fe–Al phase diagram, a stoichiometric concentration of 25 at.% Al is related to a sharp non-symmetric peak in hardness [21,22]. Furthermore, higher ductility at lower temperatures is expected for $D0_3$-ordered Fe_3Al compared to B2-ordered FeAl with more than 42 at.% Al. This advantage arises from a rather continuous BDTT in binary $D0_3$ alloys where ductility continuously increases with temperature [23]. Alloying by Mo and Ti was shown to lead to a substitutional solid-solution in near-Fe_3Al alloys [24] where they preferentially substitute for Fe on β-Fe atom positions [25]. In numerous studies, it was proven that adding Mo and Ti to ternary Fe–Al-X alloys contributes to solid-solution strengthening, especially in the temperature range of the yield strength anomaly (YSA) and at higher temperatures [16,19,26]. Moreover, Mo and Ti induce order strengthening by shifting the $D0_3 \leftrightarrow B2$ ordering reaction to higher temperatures [27,28]. Fe–Al alloys with Mo additions especially proved effective in increasing wet corrosion resistance [29,30], but also suffered from increased brittleness at room temperature [19,25]. The motivation to add B is usually driven by the formation of strengthening particles with impurity atoms which were shown to improve high-temperature strength [31,32]. In addition, TiB_2 particles are said to significantly refine grain structures and prevent grain growth by pinning grain boundaries [33]. Still, the combined use of Mo, Ti and B has led to irregularities in the microstructural development. Mixtures with 2–4 at.% Mo and 1 at.% TiB_2 formed a ternary MoFeB eutectic phase with differing compositions [4,19,20]. These findings point towards a high affinity of Mo to form precipitates in the presence of B, with a consequently reduced solid solution. Despite the beneficial effects of Mo alloying, cracking is a severe problem in the production of cast parts [19]. Neither its sensitivity to Al concentrations around the Fe_3Al hardness peak nor the effect of B concentration on the particle formation dynamics was examined. Therefore, an optimization of the Fe_3Al–Mo–Ti–B system in terms of high-temperature strength and room temperature ductility is favorable.

The objective of the study was to investigate the sensitivity of the Fe–Al–Mo–Ti–B alloy system on alloying content variations. By systematically changing Mo and B contents for two near-Fe_3Al alloys, we aimed at deepening the understanding of the role of multiple alloying additions in $D0_3$ structured iron aluminides. This included the combined effect of alloy additions on microstructure evolution, phase stability and mechanical properties and if their effect varies below and above the stoichiometric composition. Therein, we address the questions of how different alloy concentrations affect grain size, solid-solution formation and secondary phase fractions and how it translates into hardness and tensile properties at room temperature and near the YSA. A special focus is directed towards the effectiveness of solid-solution hardening by the combined use of Mo and Ti.

2. Materials and methods

For the alloy system of Fe-xAl-yMo-0.5Ti-zB, eight alloy compositions were selected (see Table 1) for mechanical and microstructural characterization. The alloys were made from pure Fe (99.8 wt%, PURON Metals, Germany), high-purity Al (99.998 wt%, Norsk Hydro ASA, Norway) and master alloys Fe-36.4Mo (wt.%, IME RWTH Aachen, Germany), Fe-72.2Ti (wt.%, Otto Junker GmbH, Germany) and Fe-19.6B (wt.%, Otto Junker GmbH, Germany). Alloys were produced by centrifugal investment casting (IC) into insulated ceramic molds made from Al_2O_3. The melts were homogenized for 2 min under vacuum and the molds were preheated to a minimum of 1000 °C before casting. After centrifugal casting, the hot molds were cooled in a preheated furnace to room temperature to minimize cracking. Actual compositions were measured by x-ray fluorescence (XRF) spectroscopy using a calibrated NitonTM XL3t GOLDD + XRF analyzer by Thermo Fischer Scientific. Spark optical emission spectroscopy (S-OES) was additionally used for determining boron concentrations. The measurements were conducted on a SPECTROTEST TXC35 mobile metal analyzer by SPECTRO Analytical Instruments calibrated on a Fe–Al–Mo–Ti–B reference alloy. Nominal and actual compositions of alloys x-y-z (with x, y, z indicating nominal alloy contents in Fe-xAl-yMo-0.5Ti-zB) are listed in Table 1.

Samples for microstructural analysis and hardness testing were taken from casting slabs with wall thicknesses of around 20 mm. Samples of all alloys were cut by a diamond blade with water cooling. For grain size analysis, microsections were ground and polished down to a minimum diamond grain size of 3 μm and etched by Adler solution (25 ml distilled water, 50 ml HCl (32%), 15 g $FeCl_3$, 10 g $(NH_4)_2CuCl_4$) to reveal the grain contrast. Images were taken by optical microscopy (OM) on a Zeiss Axiotech 100 HD microscope with a Zeiss Axiocam 503 in brightfield mode. The grain sizes were estimated by the Heyn lineal intercept procedure following ASTM E 112 [34]. The mean lineal intercept lengths were averaged in two directions and translated to average grain diameters according to DIN EN ISO 643 [35].

For microstructural investigations, microsections were polished down to 1 μm grain size and finished in non-crystallizing oxide polishing suspension from Struers. Microstructures were investigated in a Zeiss LEO Gemini 1530 VP scanning electron microscope (SEM) equipped with a field emission gun and a backscattered electron (BSE) detector. Elemental compositions of phases present were examined by wavelength-dispersive spectroscopy (WDS) using a JEOL JXA-8900 RL microprobe analyzer at a voltage of 12 kV and a current of 20 nA. Multiple spot measurements of individual phases were conducted to translate element count signals into weight percentages per linear regression. The concentrations were derived from pure element standards (except for boron). Mean matrix compositions were obtained from mappings, whereas boride concentrations were averaged from multi-spot analysis.

The present main phases and the ordering of the matrix phase were determined by conventional transmission electron microscopy (TEM). Samples were cut to a starting thickness of around 1 mm before grinding them down to a thickness of about 150 μm. Small disks with a diameter of 3 mm were punched out of the ground slices and electropolished with a Struers Tenupol-3 electropolishing unit. An electrolyte solution of perchloric acid (6%), 2-butoxyethanol (35%) and methanol (59%) was prepared for electropolishing at 50 V and −4 °C. Bright-field (BF) images of different phases and selected area electron diffraction (SAD) patterns were acquired with a JEOL JEM-2200FS TEM equipped with a field emission gun and working with an acceleration voltage of 200 kV. The

Table 1
Nominal and actual composition (measured by XRF spectroscopy and spark OES*) of Fe-xAl-yMo-0.5Ti-zB alloys in as-cast state.

Alloy x-y-z	Nominal composition (at.%)					Actual composition (at.%)				
	Fe	Al (x)	Mo (y)	Ti	B (z)	Fe	Al (x)	Mo (y)	Ti	B* (z)
26-4-1	68.5	26	4	0.5	1	69.0	26.0	3.5	0.5	1.0
26-4-0.5	69.0	26	4	0.5	0.5	69.2	26.3	3.6	0.5	0.5
26-2-1	70.5	26	2	0.5	1	69.8	26.8	1.8	0.5	1.1
26-2-0.5	71.0	26	2	0.5	0.5	70.8	26.4	1.8	0.5	0.5
23.5-4-1	71.0	23.5	4	0.5	1	71.1	23.9	3.5	0.5	1.0
23.5-4-0.5	71.5	23.5	4	0.5	0.5	71.5	24.1	3.5	0.5	0.5
23.5-2-1	73.0	23.5	2	0.5	1	72.0	24.6	1.8	0.5	1.1
23.5-2-0.5	73.5	23.5	2	0.5	0.5	72.6	24.6	1.8	0.5	0.5

expected diffraction patterns were additionally simulated by JEMS electron microscopy simulation software (2018, 21st build) [36] and compared against experimental patterns.

For the estimation of secondary phase fractions, microsections were etched with an alkaline solution (50 ml distilled water, 2 g NaOH, 1 g KOH) to enhance the phase contrast. Images were taken in bright field mode on a Zeiss Axioscope 5/7/Vario equipped with an Axiocam 506. The secondary phases were segmented by image thresholding using the image analysis software FIJI (Version 1.53c) [37]. Images were transformed to 8-bit greyscale followed by auto thresholding with the Otsu or Yen method. A minimum of 25 images (each 519 × 408 μm^2) were analyzed and qualitatively checked as overlays of the original.

Phase transition and melting temperatures were obtained by differential thermal analysis (DTA) using a thermobalance Setaram TAG24 equipped with a DTA measuring head. The measurements were conducted in flowing argon ($\approx 35 \cdot 10^{-5}$ l s^{-1}) after repeated evacuation using covered alumina-crucibles at a heating rate of 10 K min^{-1} up to a maximum temperature of 1600 °C. Cooling to room temperature was also carried out at −10 K/min. Heating and cooling cycles were repeated twice to be able to recognize irreversible transformation and verify transition temperatures.

The macrohardness was measured at room temperature on a KB 30 SR FA Basic hardness tester. A Vickers indenter at 10 kg loading was used and a total of 18 indents were performed per alloy according to DIN EN ISO 6507-1 [38]. The lens optics and hardness outputs were checked against a standardized test block before testing. Likewise, the microhardness with a Vickers indenter and a reduced load of 0.01 kg was measured on a Qness 60 A + EVO hardness tester. HV0.01 microhardness was only determined in the $D0_3$ Fe_3Al matrix.

Casting blanks with a wall thickness of 18.5 mm were extracted from casting bodies by water jet cutting. For high-temperature tensile testing, a heat treatment of 1000 °C for 100 h (HT2) followed by furnace cooling was applied for homogenization of the microstructure. Blanks were turned into cylindrical tensile specimens with a gauge length of 50 mm and a diameter of 10 mm. Tensile tests were performed according to DIN EN ISO 6892-1 [39] and −2 [40] for room and high temperature (550 °C) testing at a constant strain rate of $2.5 \bullet 10^{-4}$ s^{-1}. Tests at 550 °C were conducted in a fully enclosing, insulated furnace and gauge length ends were equipped with thermocouples monitoring the temperature throughout the test. If not otherwise stated, two tensile specimens from the same batch were tested per alloy and test temperature.

3. Results and discussion

3.1. Microstructure and phase evolution in investment cast Fe–26Al–4Mo-0.5Ti–1B

For a thorough identification of phases in the near Fe_3Al–Mo–Ti–B system, the alloy with a composition of Fe–26Al–4Mo-0.5Ti–1B (alloy 26-4-1) was considered as base alloy and studied in more detail in terms of microstructure. The microsection of alloy 26-4-1 is displayed in a light microscopic image in Fig. 1a. The left and right regions were in contact with the casting mold. Adler etching revealed grain areas with different orientations. Notably, a non-uniform grain structure resulted from centrifugal investment casting. Columnar-like grains can be recognized growing from the outer casting walls towards the center, where grains possess a mostly non-equiaxed and irregular morphology typical for cast structures.

Fig. 1b shows an SEM-BSE image with phase contrast of the as-cast condition. It mainly consists of the Fe_3Al matrix and a eutectic structure, which comprises a lamellar secondary phase (bright) surrounded by Fe_3Al (grey). The secondary phase is a complex boride which was assigned to the Mo_2FeB_2 structure according to Li et al. [20]. WDS elemental compositions of both phase constituents are listed in Table 2. Due to alloying additions, the Fe_3Al matrix builds a solid solution with Mo (2.4 at.%) and Ti (0.7 at.%). Mo_2FeB_2-type borides show an

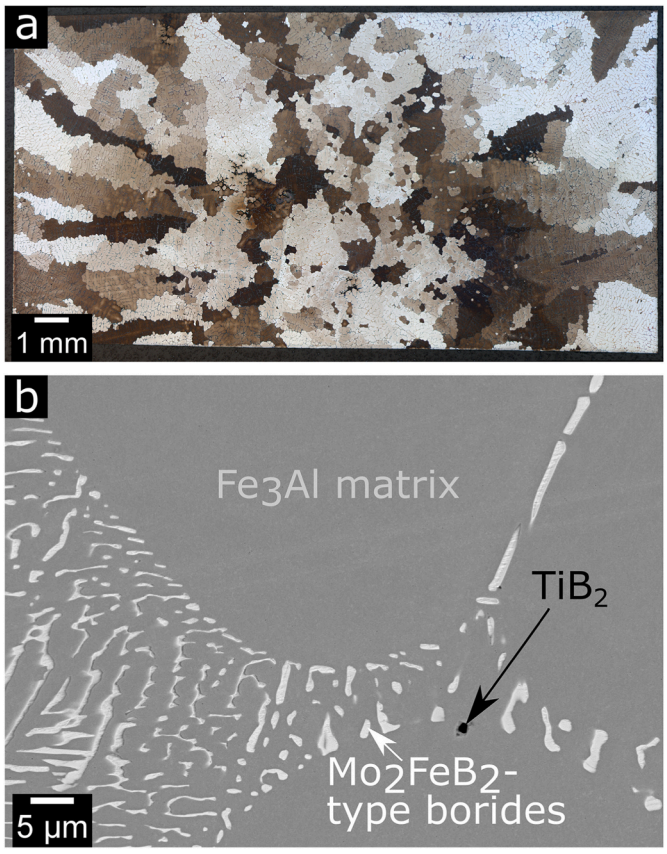

Fig. 1. Representative microsection images of investment cast Fe–26Al–4Mo-0.5Ti–1B in as-cast state with a wall thickness of 20 mm: (a) Optical micrograph of grain structure along the complete wall thickness (i.e. along the horizontal), (b) high-magnification SEM-BSE image of the main phase constituents.

Table 2
Elemental compositions of matrix (Fe_3Al) and secondary boride phase (Mo_2FeB_2) in as-cast Fe–26Al–4Mo-0.5Ti–1B measured by WDS.

Phase			Elemental composition (at.%)				
			Fe	Al	Mo	Ti	B
Fe_3Al	as-cast	This work	70.3	26.6	2.4	0.7	–
	1000 °C, 100 h, furnace-cooled	Li et al. [20]	69.6	26.9	3.2	0.34	–
Mo_2FeB_2	as-cast	This work	23.7	1.4	29.7	6.7	38.5
	1000 °C, 100 h, furnace-cooled	Li et al. [20]	25.2	0.5	36.8	8.3	29.2

off-stoichiometric Mo:Fe ratio with a high Ti fraction and small additions of Al. The lower Mo concentration is assumed to arise from the small boride phase volume which enhances matrix effects from surrounding Fe_3Al. STEM-EDS measurements of borides (not shown here) pointed towards a Mo:Fe ratio of 2:1 as expected. Besides the main phases, dark spherical precipitates marked by a black arrow in Fig. 1b were occasionally observed, but the fraction is minor. WDS measurements indicated particles with TiB_2 composition with additions of Mo.

Conventional TEM was used to identify the phases present in the matrix and boride. Fig. 2 summarizes the results of the phase analysis. Fig. 2a and b depict the BF images of the two main phase constituents which were analyzed by SAD (Fig. 2c and d). The selected area aperture positions are indicated by gray dashed circles and indicate approximately the interaction volume for diffraction. For better visualization, SAD patterns are displayed with inverted contrast. The diffraction

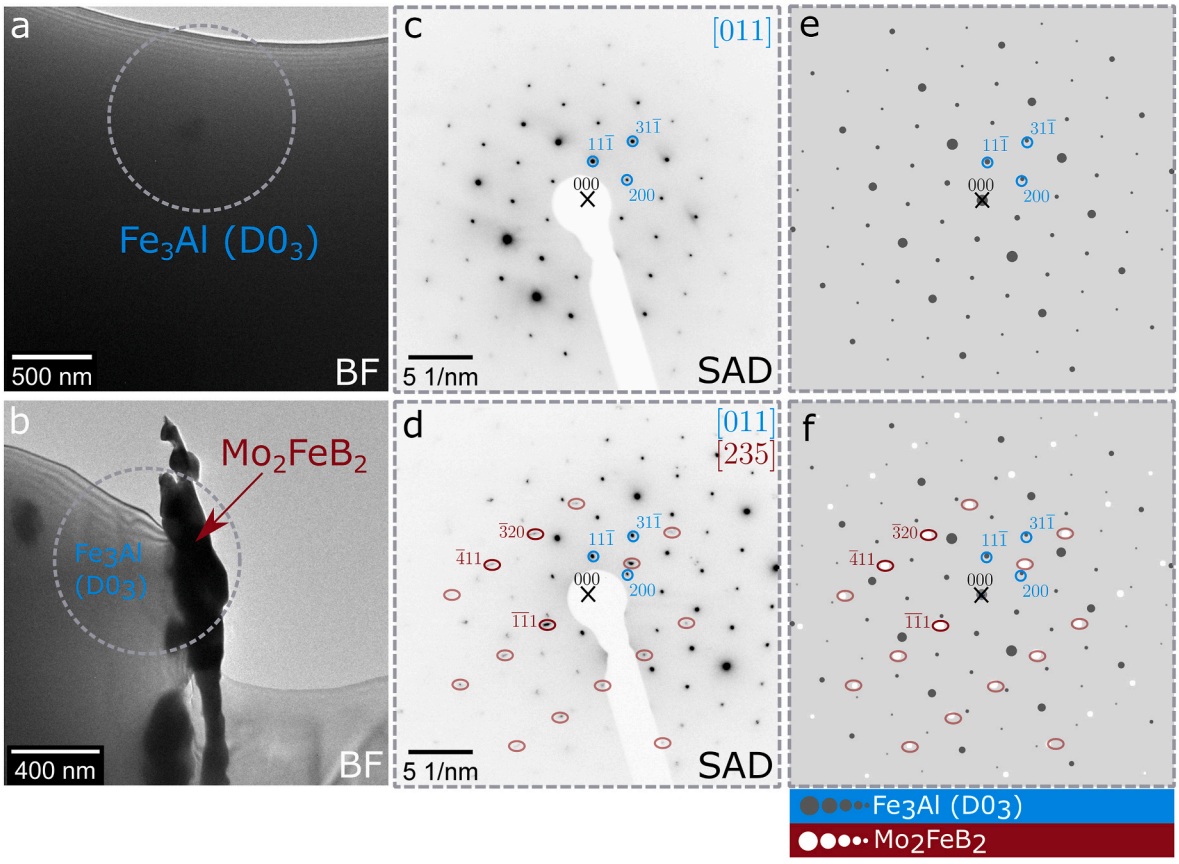

Fig. 2. Phase analysis of Fe–26Al–4Mo-0.5Ti–1B by transmission electron microscopy for matrix (a,c,e) and eutectic borides (b,d,f): Bright field (BF) images of the alloyed Fe_3Al matrix (a) and the Mo_2FeB_2 phase (b). (c,d) Inverted selected area electron diffraction (SAD) patterns generated from the areas indicated by dashed circles in a and b. Zone axes were determined as [011] for Fe_3Al (c,d) and [235] for Mo_2FeB_2 (d). Image d is a superposition pattern of the Fe_3Al (blue circles) and Mo_2FeB_2 phase (red ovals). (e,f) Simulated diffraction patterns of the crystal structures of binary Fe_3Al (dark spots) and Mo_2FeB_2 (bright spots). Diffraction patterns correspond to the same zone axes and scale as in images c and d. Indexed reflections from experimental patterns in c and d are superimposed for comparison.

pattern of the Fe_3Al matrix was indexed using the ordered cubic $D0_3$ structure (Fm-3m, space group 225) [41]. The corresponding SAD pattern in Fig. 2c matches the [011] zone axis. The B2 phase can be excluded based on the presence of weak superlattice reflections (indexed here to $D0_3$ $(11\bar{1})$ and $(31\bar{1})$ which are forbidden in the B2 structure [42]. The $D0_3$ order is also confirmed by the simulated pattern of binary Fe_3Al reproduced by JEMS and displayed in Fig. 2e. The superimposed experimental indexes of $(11\bar{1})$ and (200) fit well with the theoretical positions of reflexes.

For the boride phase, the tetragonal crystal structure for Mo_2FeB_2 proposed by Gladyshevskii et al. (P 4/m b m, space group 127) [43] was assumed. The investigated boride lamella was located at a grain boundary (see Fig. 2b). Fig. 2d represents the respective SAD pattern showing a superposition of $D0_3$ Fe_3Al in the [011] zone and the boride. Reflections of the boride phase which fit the Mo_2FeB_2 structure are highlighted by red ovals. The reflections found suggest an orientation close to the [235] zone axis. The simulation of both patterns in the respective zone axes is displayed in Fig. 2f. Overlayed indexed positions of the boride from experiments indicate a good match with theoretical positions of Mo_2FeB_2.

3.2. *Microstructure and phase evolution in Fe-xAl-yMo-0.5Ti-zB alloys*

Microsections of all alloy variations Fe-xAl-yMo-0.5Ti-zB (denoted as alloy x-y-z) in the as-cast state were investigated by OM, SEM and hardness testing. As was displayed in Fig. 1a, individual grain sizes vary considerably, from several tens of microns to more than a few millimeters. This heterogeneous grain size distribution is reflected in measured average grain sizes and their scatter in all as-produced alloy variations. Average grain diameters and the 95% confidence intervals (CI) from Heyn lineal intercept counting are listed in Table 3. Because of the irregular grain shape, the confidence interval of calculated average grain diameters is very large. Average grain sizes span from 586 μm (alloy 23.5-4-0.5) to 876 μm (alloy 26-2-1) for a mean wall thickness of 20 mm. The evolution of large grains is favored by low heat transfer rates by insulated ceramic shell molds and consequently low cooling rates within the melt. Nevertheless, average grain sizes agree well with other FeAl alloys produced by investment casting [44]. No systematic correlation of grain size with varying alloy composition can be deduced from the data.

Representative SEM-BSE images of all alloy compositions are compared for alloys with 26 at.% Al in Fig. 3 and for 23.5 at.% Al in Fig. 4. Additionally, elemental compositions of matrix and borides as

Table 3
Average grain diameters and 95% confidence intervals of investment-cast Fe-xAl-yMo-0.5Ti-zB determined by Heyn lineal intercept procedure.

Alloy x-y-z	Average grain diameter (μm)
26-4-1	602 ± 121
26-4-0.5	740 ± 155
26-2-1	876 ± 167
26-2-0.5	696 ± 188
23.5-4-1	745 ± 117
23.5-4-0.5	586 ± 66
23.5-2-1	748 ± 152
23.5-2-0.5	715 ± 93

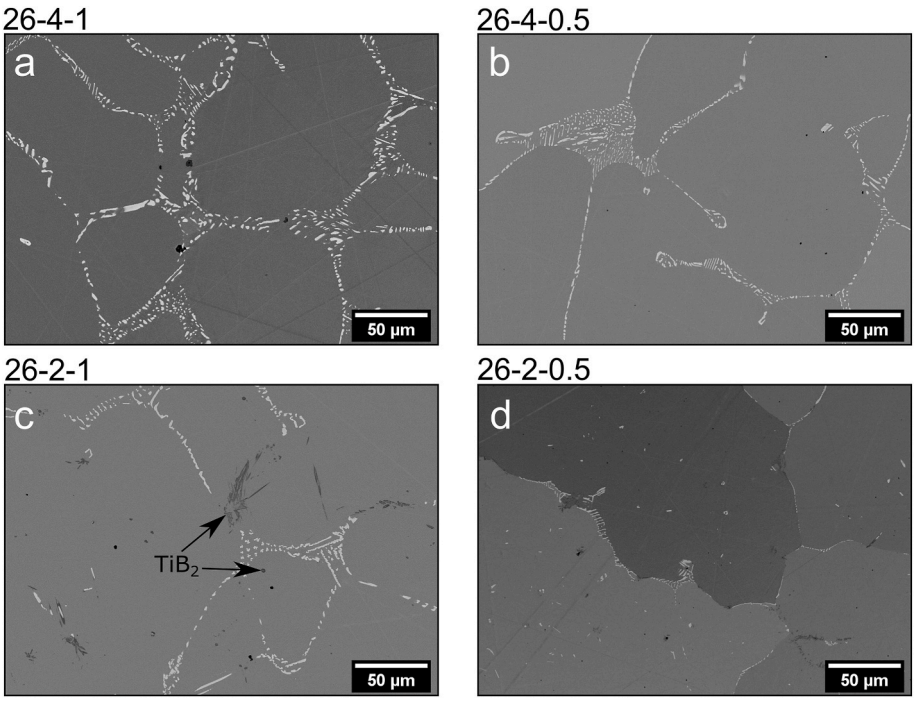

Fig. 3. SEM-BSE images of as-cast Fe–26Al-yMo-0.5Ti-zB alloys (26-y-z).

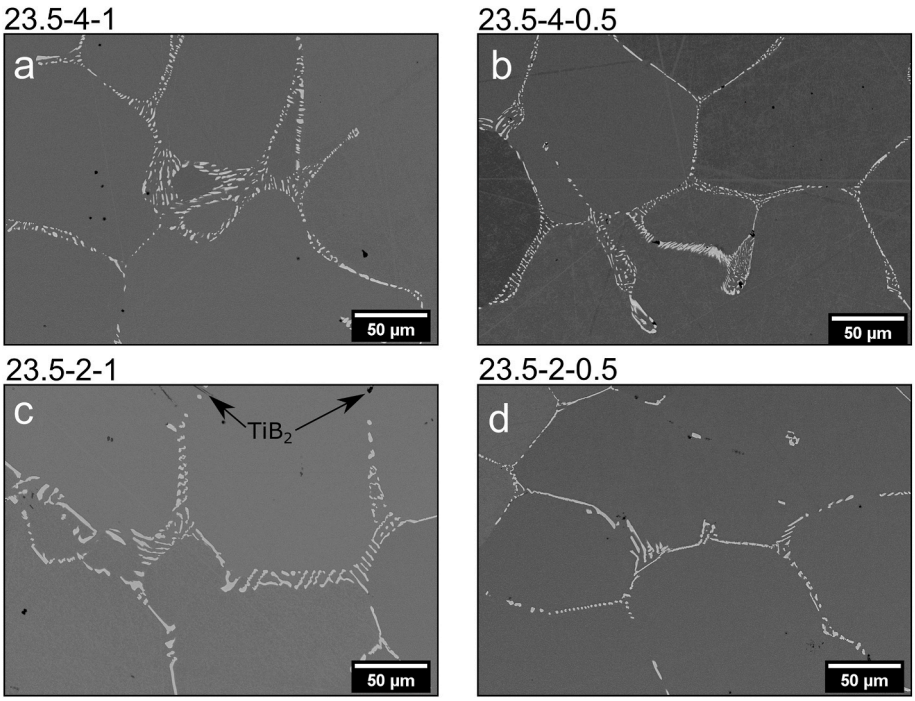

Fig. 4. SEM-BSE images of as-cast Fe-23.5Al-yMo-0.5Ti-zB alloys (23.5-y-z).

measured by WDS are summarized in Table 4. Variation of nominal Mo content induces a change in solid-solution concentration. At nominally 2 at.% Mo, Mo concentrations range between 1.2 and 1.3 at.% in the Fe_3Al matrix. These concentrations agree well with measurements by Li et al. [20] and McKamey et al. [19]. Within this concentration range, they attested that the amount of Mo going into solid solution with Fe_3Al scales with the total Mo concentration in the alloy. Concerning boride composition, Ti concentrations generally increase when nominal Mo contents are lowered. Moreover, other secondary phases tend to be increasingly present with reduced Mo content (see Fig. 3c and d and Fig. 4c and d).

Besides spherical precipitates which are already observed in 26-4-1 alloys, dark acicular precipitates formed after casting. Point analysis indicates a similar composition as for spherical precipitates. Moszner et al. [4] made similar findings on powder metallurgical Fe-25.3-2.0Mo-0.5Ti-1.4B in which they identified Ti-rich borides and carbides. The increased fraction of Ti-rich precipitates persisted with nominally lower B content. Generally, reduced alloy additions of B (0.5

Table 4
Elemental compositions of Fe_3Al matrix and Mo_2FeB_2 borides in as-cast alloy variants analyzed by WDS.

Alloy x-y-z	Elemental composition (at.%)								
	Fe_3Al matrix				Mo_2FeB_2 boride				
	Fe	Al	Mo	Ti	Fe	Al	Mo	Ti	B
26-4-1	70.3	26.6	2.4	0.7	23.7	1.4	29.7	6.7	38.5
26-4-0.5	69.9	26.7	2.6	0.8	23.8	2.0	28.2	6.4	39.6
26-2-1	71.5	26.9	1.2	0.4	23.9	0.5	27.1	9.7	38.9
26-2-0.5	71.3	26.7	1.3	0.7	25.7	2.0	25.1	8.6	38.6
23.5-4-1	72.7	24.1	2.5	0.7	24.7	1.2	30.2	6.8	37.1
23.5-4-0.5	72.4	24.1	2.7	0.8	24.3	1.5	29.7	6.6	37.9
23.5-2-1	74.0	24.2	1.2	0.6	24.0	0.8	26.9	9.5	38.9
23.5-2-0.5	73.5	24.5	1.2	0.7	23.5	0.3	26.9	10.4	38.9

at.%) were accompanied by a refinement of the eutectic boride network (i.e. boride lamellae decreased in apparent size and fraction). Only minor compositional changes of matrix and borides of <10 rel.% occurred. For variation of nominal Al content, the concentration of Al in the matrix is mainly affected. 23.5-y-z alloys amount to on average 24.2 at.% Al against 26.7 at.% in 26-y-z alloys. Besides, elemental compositions of matrix and borides did not considerably differ by varying between 23.5 and 26 at.% Al.

As phase fractions of borides and Ti-rich precipitates appear to differ in all alloys, secondary phase fractions were quantified by OM and image processing. To enhance the contrast and contouring of the matrix and secondary phases, metallographic surfaces were prepared by an alkaline etchant. Yet, its use inhibited the differentiation of borides and Ti-rich precipitates under OM. Therefore, the sum of all secondary phase fractions was acquired. Average area fractions of secondary phases in all alloys are summarized in Fig. 5. According to the Delesse principle, area fractions should correspond to volume fractions if a random orientation of secondary phases is assumed [45]. Bars in the plot are sorted in descending order of their nominal alloy concentrations for Al (x), Mo (y), and B (z). Thereby, secondary phase area fractions vary between 1.4 and 2.6%. Area fractions scale with increasing nominal content of Mo and B. From this correlation, it can be concluded that the refinement of eutectic borides, as was observed in alloys x-y-0.5 with reduced nominal B content (Fig. 3b, d and Fig. 4b, d), can be related to a general decrease of secondary phase fractions. Moreover, nominally less Mo promotes the preferential formation of TiB_2 precipitates at the expense of eutectic borides. In addition, secondary phase fractions decrease overall. Against this, changing the Al content around stoichiometric Fe_3Al composition

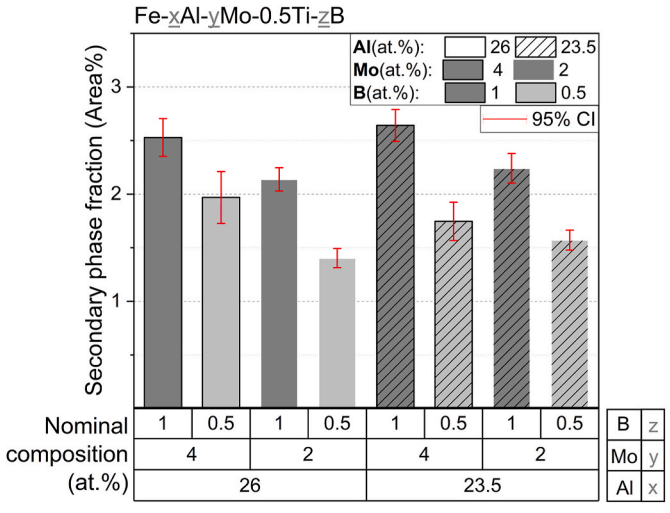

Fig. 5. Secondary phase fractions dependent on nominal alloy composition determined by optical microscopy and image thresholding. Secondary phases comprise both eutectic borides and TiB_2 precipitates.

does not affect secondary phase fractions.

Differential thermal analysis was conducted to derive temperatures of phase transitions. Based on these transition temperatures, the identity of the present phases can be verified. Moreover, the effect of alloying concentrations on phase stabilities can be investigated. DTA heating curves of all alloy variants are depicted in Fig. 6. The curves are shifted along the vertical axis for better illustration. They are split into temperature regions for solid-state transformations (Fig. 6a) and melting transitions (Fig. 6b). Detectable solid-state transformation of Fe_3Al in all alloys are the order-order transitions $D0_3$ to B2 ($T_c^{D03\leftrightarrow B2}$) and the order-disorder transitions B2 to A2 ($T_c^{B2\leftrightarrow A2}$). They are second-order transitions and therefore defined at the local minima representing an endothermic peak in the heating curves. $T_{solidus}$ and $T_{liquidus}$ confine the melting interval of the eutectic and matrix phase and represent first-order transition temperatures. $T_{solidus}$ is referred to as the onset of the first melting peak and corresponds to the eutectic melting temperature. The point of onset is determined by two intersecting tangents which are exemplarily shown in Fig. 6b. $T_{liquidus}$ here refers to the endothermic peak with the highest temperature within the melting interval and marks the temperature at which melting is completed. Liquidus temperatures were compared with the equivalent onset temperatures for solidification in the cooling curves, which show good agreement. All transition temperatures are summarized in Table 5. Transition temperatures for binary Fe–25Al and Fe–27Al [46] are additionally included.

In comparison to binary Fe–Al, all alloys exhibit a shift of $T_c^{D03\leftrightarrow B2}$ and $T_c^{B2\leftrightarrow A2}$ towards higher temperatures due to alloying additions of Mo and Ti [19,47]. With varying additions of Al and B, $T_c^{D03\leftrightarrow B2}$ shifts between 54 and 78 K with 2 at.% Mo or 110–130 K with 4 at.% Mo. In alloys with reduced B (x-y-0.5), the systematic increases of $T_c^{D03\leftrightarrow B2}$ can be also correlated to higher solute concentrations of Mo as determined by WDS (see Table 4). The average increase of $T_c^{D03\leftrightarrow B2}$ (58 K) by doubling the nominal Mo content (i.e. from 2 to 4 at.%) is higher than the average increase of $T_c^{B2\leftrightarrow A2}$ (25 K). The absolute shift of $T_c^{B2\leftrightarrow A2}$ is more influenced by Al content. Thereby, $T_c^{B2\leftrightarrow A2}$ is located between 784 and 823 °C for 23.5 at.% Al and 888–921 °C for 26 at.% Al. The reduction of the order-disorder transition temperature with lower Al content is consistent with the shift of the B2↔ A2 phase transition towards lower temperatures in binary alloys [46]. Likewise, the order-order transition temperature ($D0_3$ ↔ B2) decreases on average by 12 K by lowering Al contents from 26 to 23.5 at.%. In binary $D0_3$ structured Fe–Al, $T_c^{D03\leftrightarrow B2}$ is nearly constant in the considered composition range (see Table 5). Hence it could be speculated that solid-solution additions in $D0_3$ structured Fe–Al tend to increase the dependency of the phase transition temperature on Al concentration. Concerning potential A2 phases in 23.5-x-y alloys, the presence of both $T_c^{D03\leftrightarrow B2}$ and $T_c^{B2\leftrightarrow A2}$ in alloys with nominal 23.5 at.% Al confirms the absence of disordered A2 phases at room temperature.

About first-order transitions, the melting interval of all alloys is widened against binary alloys due to the additional melting of eutectic borides. Notably, alloys x-4-z and x-2-z differ by the number of endothermic peaks during melting. While alloys x-4-z have two peaks, alloys x-2-z exhibit an additional third reaction at $T^*_{solidus}$ (see Fig. 6b). For alloys with 2 at.% Mo, $T^*_{solidus}$ ranges from 1326 to 1349 °C and $T_{solidus}$ from 1353 to 1362 °C. For alloys with 4 at.% Mo, the onset of melting $T_{solidus}$ ranges between 1360 °C and 1370 °C. Besides, the enthalpies of the melting peaks (i.e. the peak areas enclosed by an interpolated baseline) at $T_{solidus}$ decrease with reduced B and Mo contents. As this decrease in enthalpy correlates with the apparent decrease of eutectic boride phase fractions in Figs. 3 and 4, it is plausible that this temperature range corresponds to the melting of the eutectic. The origin of $T^*_{solidus}$ of x-2-z alloys, in turn, can be potentially associated with the dissolution of TiB_2 particles, which increase in apparent fraction at lower Mo contents.

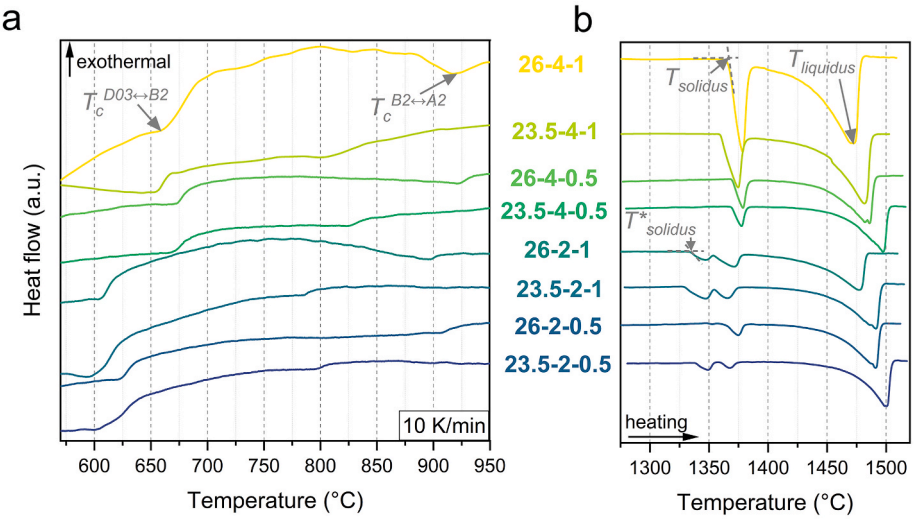

Fig. 6. DTA heating curves of all alloy variants with a constant heating rate of 10 K/min. Temperature ranges are separated by solid-state transformations (a) and for melting transitions (b).

Table 5
Phase transition temperatures of Fe-xAl-yMo-0.5Ti-zB alloys determined by DTA.

Alloy x-y-z	$T_c^{D03\leftrightarrow B2}$ (°C)	$T_c^{B2\leftrightarrow A2}$ (°C)	$T^*_{solidus}$ (°C)	$T_{solidus}$ (°C)	$T_{liquidus}$ (°C)
26-4-1	662	917	–	1367	1473
23.5-4-1	652	812	–	1360	1482
26-4-0.5	673	921	–	1370	1486
23.5-4-0.5	665	823	–	1369	1497
26-2-1	604	888	1334	1353	1477
23.5-2-1	596	784	1326	1354	1491
26-2-0.5	621	907	1349	1362	1491
23.5-2-0.5	601	794	1339	1355	1500
Fe–27Al [46]	543	868	–	1482	1500
Fe–25Al [46]	542	753	–	–	–

3.3. Mechanical properties in Fe-xAl-yMo-0.5Ti-zB alloys

Fig. 7a compares the HV10 macrohardness of all eight alloys. As diagonals of Vickers indents amount to more than 200 μm, hardness was effectively probed on the combined microstructure of the Fe_3Al matrix and borides. Macrohardness ranges from 281 to 344 HV10 dependent on alloy composition. With respect to 26-y-z alloys, macrohardness varies between 281 and 296 HV10. Literature values of binary, $D0_3$ structured Fe-27.9Al produced by vacuum induction melting state a hardness of 299 HV5 [48].

It appears surprising that the investigated alloys strengthened by borides and solid solution show comparable hardness to unalloyed Fe–28Al. We assume that the comparably low hardness of alloy variations arises from the higher testing force and weaker grain boundary strengthening as was revealed by large average grain sizes (see Table 3). The effect of grain boundary strengthening on yield strength and therefore hardness in iron aluminides was already reported [49] and therefore could explain the lower hardness measured. Notably, all alloys with a nominal Al content of 23.5 at.% show increased hardness compared to alloys with nominal 26 at.% Al. In direct comparison of alloys with fixed Mo and B content, alloys with 23.5 at.% Al have on average 14 rel.% higher macrohardness than their counterparts with 26 at.% Al. To check the contribution of Fe_3Al strength on overall macrohardness, the microhardness of the Fe_3Al matrix was measured.

Fig. 7b reports the HV0.01 values similarly to Fig. 7a. Note that absolute HV0.01 values are higher compared to HV10 values due to the indentation size effect [50,51]. Less variation of hardness values occurs

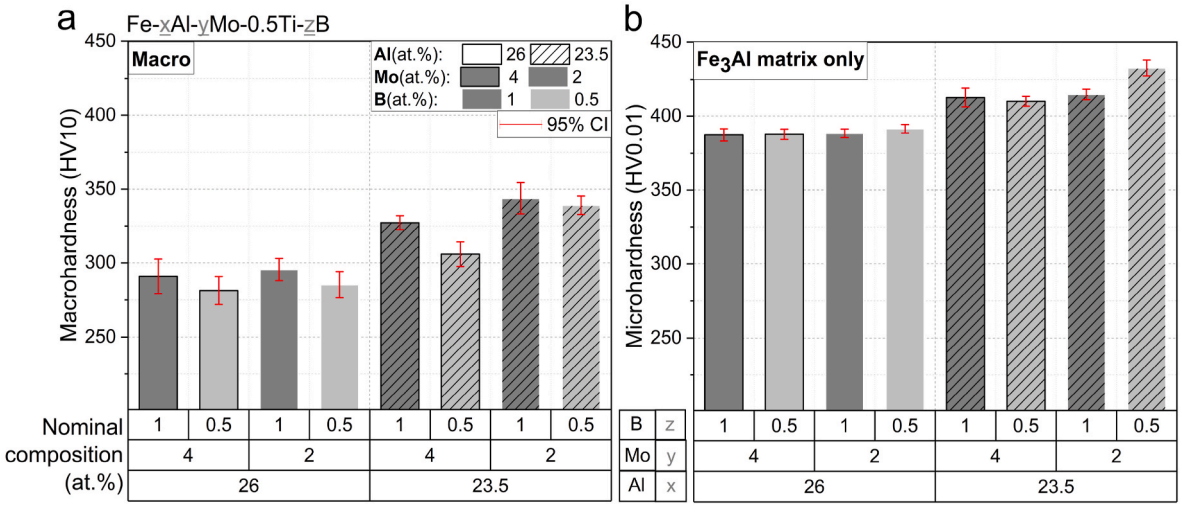

Fig. 7. Mean HV10 macrohardness (a) and mean HV0.01 microhardness of Fe_3Al matrices (b) of as-cast Fe-xAl-yMo-0.5Ti-zB alloys.

upon changing Mo or B contents. Alloys with 23.5 at.% Al (417 ± 10 HV0.01) exceed average microhardness of 26-y-z alloys (389 ± 2 HV0.01) suggesting higher strength in 23.5-y-z alloys. Our data match the Al-dependent yield strengths of binary alloys near Fe_3Al stoichiometry found in experiments [21,22]. For binary alloys below 25 at.% Al, a local maximum of yield strength exists. Around this strength maximum, yield strengths at lower Al concentrations decrease less than at higher concentrations. Accordingly, it can be assumed that 23.5-y-z alloys belong to the higher yield strength regime. This agreement of yield strength relations in binary and alloyed Fe_3Al could suggest that solid-solution additions do not affect the yield strength evolution with Al concentration. Regarding the other alloy additions, macrohardness tends to scale with increasing nominal B content. This correlates with the increase of the secondary phase fraction (i.e. the eutectic phase fraction) in Fig. 5. Microhardness measurements within the eutectic phase region in alloy 26-4-1 (not shown here) pointed towards a 50 rel. % higher hardness compared to the Fe_3Al matrix. Consequently, it appears plausible that a refinement of the eutectic phase and a reduction of borides is accompanied by a decreased hardness. As no incorporation of B into Fe_3Al was found according to WDS, a change of matrix hardness upon different B contents was not expected and generally not seen. The unexpected rise of matrix hardness in alloy 23-2-0.5 remained without causal explanation. Concerning variations of Mo content, the microhardness of Fe_3Al remained constant independent of Mo content. Likewise, macrohardness was not affected by less Mo or even slightly increased (alloy 23.5-2-1).

To verify the effect of alloy elements on mechanical properties, tensile tests at room temperature and 550 °C were performed. The higher test temperature coincides with the estimated temperature of maximum yield strength relating to the yield strength anomaly (YSA) of FeAl alloys [20]. Note that the respective YSA temperatures of the other alloys could slightly shift due to different alloying contents [18]. Fig. 8a and b displays the mean 0.2% proof strengths $R_{p0.2}$, if available, and ultimate tensile strengths R_m of all investigated alloys at the respective temperatures. Standard deviations are included as red error bars if mean values are displayed.

The ultimate tensile strengths of all alloy variants range from 216 MPa (alloy 23.5-4-1) to 318 MPa (alloy 23.5-2-1) at room temperature. Strength relations between alloys agree well with the hardness measurements previously shown. In terms of yielding, most alloys failed before reaching a plastic deformation of 0.2%. Two exceptions were the 26-2-z alloys which reached 0.2% proof strengths of 234 MPa (alloy 26-2-1) and 221 MPa (alloy 26-2-0.5). Consequently, they reached the highest fracture elongations among all alloys with 0.4% (alloy 26-2-1) and 0.3% (alloy 26-2-0.5).

As a comparison, the fracture elongation of cast binary Fe_3Al is given as 0.7% [23]. It can be thus concluded that the reduction of Mo is effective in reducing brittleness and recovering ductility in boride-strengthened solid-solution hardened Fe–26Al-xMo-0.5Ti-zB. As both secondary phase fractions and solid-solution concentrations diminished upon reducing Mo content from 4 to 2 at.%, one of them or both factors can contribute to reduced embrittlement. Still, secondary phase fractions also decreased upon reduction of B, which in turn did not increase ductility. This fact supports the major role of solute concentration in the Fe_3Al matrix for the gain in ductility. It also matches the fracture behavior of all alloys after testing at room temperature (not shown here). They commonly featured transgranular cleavage with surface cracks running through the matrix and detouring borides. This indicates that the matrix acts as the weakest link under tensile loading. McKamey and Horton [19] stated that ductility is continuously decreasing above a Mo content of 0.5 at.%. Interestingly, a reduction of Mo in 23.5-y-z alloys did not recover ductility and only increased strength. This comparison emphasizes how sensitive embrittlement by Mo at room temperature can be upon changing Al concentrations around Fe_3Al stoichiometry.

Mean values of $R_{p0.2}$ and R_m at 550 °C are compared in Fig. 8b. 0.2% proof strengths follow similar trends as were seen from R_m and HV10 values at room temperature. Again, the average $R_{p0.2}$ of all 23.5-y-z alloys is around 100 MPa higher than the average $R_{p0.2}$ of all 26-y-z alloys. Mean values for individual alloys with 23.5 at.% Al range between 421 MPa (alloy 23.5-4-1) and 459 MPa (alloy 23.5-2-1), while alloys with 26 at.% Al achieved between 303 MPa (alloy 26-4-0.5) and 356 MPa (alloy 26-2-1). Again, the strength especially in 26-y-z alloys is increased for higher B contents probably referring to the beneficial influence of increased secondary phase fractions. Surprisingly, the strength of 26-y-z alloys with only 2 at.% Mo is similar to alloys with 4 at.%. In 23.5-y-z alloys, $R_{p0.2}$ is even higher for reduced Mo content. The corresponding impact of solid-solution hardening will be discussed in the next section. Ultimate tensile strengths R_m at 550 °C for alloys with 26 at.% Al range between 474 MPa (alloy 26-4-0.5) and 551 MPa (alloy 26-4-1), for alloys with 23.5 at.% Al between 513 MPa (alloy 23.5-2-1) and 543 MPa (alloy 23.5-4-1). The tendency of decreased strength with reduced B content and consequently lower secondary phase fractions applies for 26-y-z alloys. Against this, strength relations based on R_m in 23.5-y-z alloys are rather not consistent but also do not show significant differences. Also note that the standard deviations of $R_{p0.2}$ and R_m at 550 °C in 23.5-y-z alloys are significantly larger than in 26-y-z alloys.

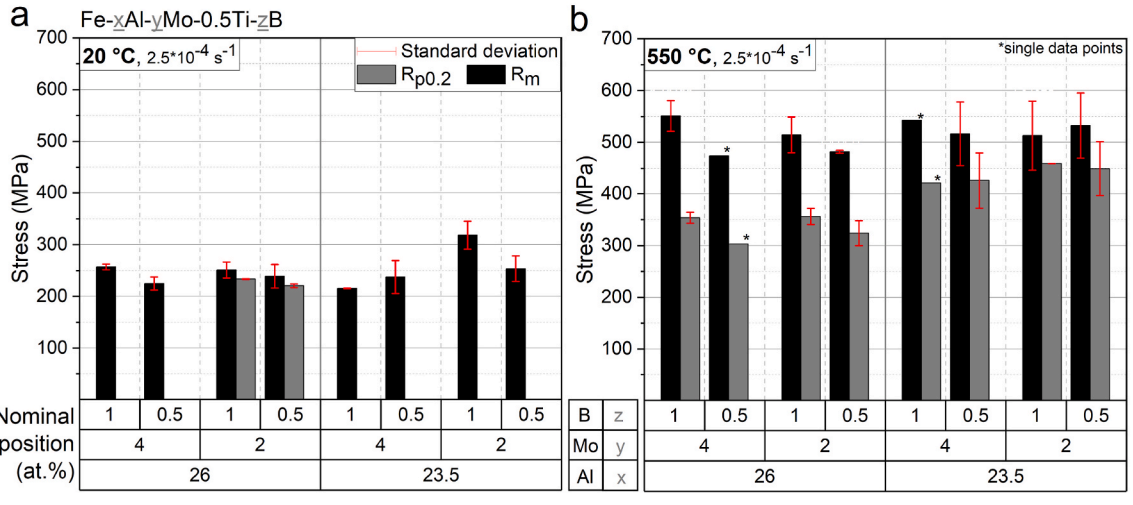

Fig. 8. Mean 0.2% proof strength $R_{p0.2}$ and ultimate tensile strength R_m at room temperature (a) and 550 °C (b) in Fe-xAl-yMo-0.5Ti-zB alloys.

3.4. Solid-solution hardening by Mo in near-Fe_3Al alloys

The results presented in the previous section indicate that no strength increase was induced by higher incorporation of Mo beyond 2 at.%. The observations on hardness and tensile strength up to elevated temperatures match reported data on comparable boride-strengthened alloys with solute Mo concentrations between 0.5 and 4 at.% [19,20]. Nonetheless, these results are opposed to the acknowledged dependency of solid-solution hardening (SSH) on solute concentration in alloys in that SSH linearly scales with solute concentration [52]. The nucleation model by Feltham is still mostly recognized for the description of solid-solution hardening in common f.c.c., h.c.p. and b.c.c. crystal systems [53]. It describes a variable power law for the dependency of the critical resolved shear stress (CRSS) on solute concentration in the form of $CRSS \propto c^r$, with r ranging from 0.5 to 1. Still, an unambiguous explanation of SSH in ordered intermetallics was shown to be difficult due to stoichiometry effects [54]. It refers to the fact that the concentration of vacancies and anti-site defects can considerably change depending on which sublattice positions solute atoms occupy. Accordingly, the mechanical behavior of solid solutions may be affected. Likewise, first-principles calculations pointed out that the electronic structure of host-solute atom pairings is decisive for the effective misfit parameters for SSH [55]. With this respect, it was demonstrated in experimental studies that different solute elements followed deviating power laws in intermetallic iron aluminides [56,57]. The single effect of Mo additions was specially addressed at higher temperatures. Palm [16] investigated compressive 0.2% proof strengths of B2 ordered Fe–26Al-xMo between 600 and 800 °C in a concentration range of up to 5 at.% Mo. He found nearly linear correlations of solute Mo concentration with 0.2% proof strength whose gradient decreased with increasing temperature. This agrees well with the nucleation model's description of thermal effects which anticipates a weaker effect of SSH at higher temperatures [52]. In turn, it could be assumed that the SSH effect at lower temperatures should not be any lower than already achieved at 600 °C. At this temperature, a jump of nearly 100 MPa in 0.2% proof strength was measured with increasing Mo contents from 2 to 4 at.%. These observations are in full contrast to the here outlined strength relations in tensile tests at 550 °C. Proof strengths in 26-2-z and 26-4-z alloys (~1.3 and 2.5 at.% Mo solute concentration in the matrix respectively) were found similar for equal B content and therefore did not show any additional SSH effect upon increasing Mo solute concentration. An increase of strength with increasing Mo concentration was also absent at room temperature according to microhardness and tensile strength.

Compounding effects such as varying grain boundary strengthening can be excluded due to very large grains in all alloys. The strengthening effect by secondary phase particles certainly varies with alloy composition. According to macrohardness and tensile strengths, lower secondary phase fractions were shown to rather decrease strength. Likewise, only a decrease in strength could be expected for alloys with less Mo content and lower secondary phase fractions, but not an increase that could compensate for SSH. To fully evaluate the hardening by the secondary phases present, one must consider further aspects such as particle size, shape and distance as well as the strengthening contributions by modulus difference of matrix and particles according to particle hardening theory [58]. Still, the alloy system cannot be easily related to conventional precipitation hardening due to the inhomogeneous distribution of secondary phases. Therefore, a thorough consideration of the particle hardening contribution is out of the scope of this work. The influence of thermal vacancy hardening at lower temperatures in investment cast 26-4-1 alloys was demonstrated to be low according to hardness measurements after vacancy removal annealing at 400 °C for 168 h (results not shown here). Nevertheless, it is unclear to which extent the capability of freezing thermal vacancies in Fe–Al alloys varies with different solute concentrations or different ratios of multiple solutes (i.e. Mo and Ti). It was only pointed out that solute species with different site preference energies indeed change the vacancy concentration [55]. In addition, it is unclear how the interaction of both solute atoms affects the total vacancy concentration. As a matter of fact, Al content and processing history were usually accounted to be mostly responsible for the number of thermal vacancies [59,60]. Therefore, it appears unlikely that equally processed Fe–Al alloys with changing alloying concentrations, but equal Al contents exhibit fundamentally different thermal vacancy concentrations in our study.

As a conclusion, the reported solid-solution hardening by Mo could saturate at a concentration below 1.2 at.% in Ti-doped near-Fe_3Al alloys. This would contradict the previous understanding of a rather linear increase of solid-solution hardening with Mo concentration. Due to the elucidated impact of additional Ti alloying, conventional solid-solution laws could fail to apply in our case. The reasons why no further hardening occurs with increasing Mo solute concentration could be related to softening effects. Phenomenological models suggested local changes of elastic moduli [61] or a decrease of Peierls' barrier [62] on the addition of solutes. Still, further analysis is required to address open questions on the contributions of particle and thermal vacancy hardening.

4. Conclusions

Eight near-Fe_3Al alloys (Fe-xAl-yMo-0.5Ti-zB) below and above stoichiometric composition have been produced by centrifugal investment casting and investigated for systematic changes of nominal alloy additions of Mo (2 and 4 at.%) and B (0.5 and 1 at.%). Correlations between combined alloy concentrations and their effect on microstructural features, phase stability and mechanical properties have been drawn. The main conclusions are as follows:

(1) All alloys mainly consist of a Fe_3Al matrix and a network of μm-sized Mo_2FeB_2 eutectic borides. The tetragonal crystal structure of the eutectic boride was confirmed by SAD. Both phases show substitution by solute elements according to WDS. Reduction of B content leads to an apparent refinement of the eutectic boride network. Minor fractions (<1 vol%) of TiB_2-type particles were also observed. With decreasing Mo content, their apparent volume fraction tends to increase, with additional precipitation of acicular particles with similar composition.

(2) Elemental compositions of phases as determined by WDS similarly vary for near-Fe_3Al alloys below and above ideal stoichiometry upon changing Mo and B concentrations. Both Mo solute concentration in the Fe_3Al matrix and secondary phase fractions scale with incorporated Mo alloy additions. Additionally, lower Mo concentrations lead to an enrichment of Ti in Mo_2FeB_2 particles, independent of B content. By reducing B content, secondary phase fractions decrease and lead to minor increases of Mo and Ti solute concentrations in the matrix.

(3) Average grain diameters from investment cast alloy variants are randomly distributed due to the casting process. No systematic changes by varying concentrations of Al, Mo and B are found.

(4) Changes to phase transitions were determined by DTA. Both order-order ($T_c^{D03\leftrightarrow B2}$) and order-disorder transition temperatures ($T_c^{B2\leftrightarrow A2}$) are generally shifted towards higher temperatures compared to binary near-Fe_3Al by solid solution with Mo and Ti. The reduction of B and the mentioned minor increases in solute concentrations can be correlated to a minor increase in ordering reaction temperatures. The dependency of $T_c^{D03\leftrightarrow B2}$ on Al concentration between nominal 23.5 to 26 at.% (actual composition between 24 and 27 at.%) is increased by alloying with Mo and Ti compared to binary alloys. The melting interval of Fe_3Al is generally increased by the additional melting of secondary phase particles. Another melting peak and an earlier onset of melting ($T^*_{solidus}$) were registered for all alloys with 2 at.% Mo. It is connected to the melting of TiB_2-type particles which were shown to increase in volume fraction within this composition.

(5) Strength relations were examined by measurements of macrohardness in ambient conditions and tensile tests at 20 and 550 °C. Strength is increased for all alloy variants with 23.5 at.% Al at room and elevated temperatures. Microhardness measurements revealed that a higher hardness of the Fe_3Al matrix is responsible as is the case for binary Fe_3Al below 25 at.%. A reduction of B and the decrease of secondary phase fractions tend to correlate with lower strength. Decreasing Mo concentration is effective in reducing brittleness and regaining ductility at room temperature. Against this, increasing Mo solute concentrations did not yield any strength increase according to solid-solution hardening theories and experimental observations with ternary Fe–Al-X alloys. It is hypothesized that the combined use of Mo and Ti as solutes could saturate solid-solution hardening or induce softening effects above 1.2 at.% Mo concentration in the matrix.

CRediT author statement

Andreas Abel: Conceptualization, Methodology, Validation, Formal analysis, Investigation, Data curation, Writing – Original draft, Visualization, Project administration Julian M. Rosalie: Investigation, Data curation, Writing – Review & Editing Stefan Reinsch: Investigation, Formal analysis, Validation Pawel Zapala: Resources, Project administration Heiner Michels: Supervision, Project administration Birgit Skrotzki: Writing – Review & Editing, Supervision, Project administration, Funding acquisition.

Funding

This joint research project was funded by the Federal Ministry for Economic Affairs and Climate Action and the German Federation of Industrial Research Associations e.V. (AiF) under project number 20965 N. The authors gratefully acknowledge the support received from the funding organizations, from the FVV (Research Association for Combustion Engines e.V.) and from all those involved in the project.

Declaration of competing interest

The authors declare that they have no known competing financial interests or personal relationships that could have appeared to influence the work reported in this paper.

Data availability

Data will be made available on request.

Acknowledgments

The authors like to thank Dan Roth-Fagaraseanu and Susanne Mosler from Rolls-Royce Germany for their continuous support during the project. Our thanks also go to the following BAM colleagues for their support in and contributions to the experiments: Steffen Thärig for performing hardness and tensile tests, Gabriele Oder for performing WDS measurements, Romeo Saliwan Neumann for providing SEM images, Markus Ostermann for analyzing elemental composition by XRF and Anna Maria Manzoni for supporting the SAD analysis.

References

[1] S.C. Deevi, V.K. Sikka, Nickel and iron aluminides: an overview on properties, processing, and applications, Intermetallics 4 (1996) 357–375, https://doi.org/10.1016/0966-9795(95)00056-9.
[2] R.R. Judkins, U.S. Rao, Fossil energy applications of intermetallic alloys, Intermetallics 8 (2000) 1347–1354, https://doi.org/10.1016/S0966-9795(00)00110-2.
[3] D.G. Morris, M.A. Muñoz-Morris, Recent developments toward the application of iron aluminides in fossil fuel technologies, Adv. Eng. Mater. 13 (2011) 43–47, https://doi.org/10.1002/adem.201000210.
[4] F. Moszner, J. Peng, J. Suutala, U. Jasnau, M. Damani, M. Palm, Application of iron aluminides in the combustion chamber of large bore 2-stroke marine Engines, Metals 9 (2019) 847, https://doi.org/10.3390/met9080847.
[5] V.K. Sikka, D. Wilkening, J. Liebetrau, B. Mackey, Melting and casting of FeAl-based cast alloy, Mater. Sci. Eng., A 258 (1998) 229–235, https://doi.org/10.1016/S0921-5093(98)00938-1.
[6] P. Kratochvil, I. Schindler, P. Hanus, Conditions for hot rolling of Fe3Al - type aluminide, Kovové Materiály - Metallic Materials 44 (2006) 321–326.
[7] V. Seetharaman, S.L. Semiatin, Powder metallurgy, in: Intermetallic Compounds: Principles and Practice, John Wiley & Sons, Chichester, UK, 2002, pp. 643–662.
[8] G. Rolink, S. Vogt, L. Senčekova, A. Weisheit, R. Poprawe, M. Palm, Laser metal deposition and selective laser melting of Fe–28 at.% Al, J. Mater. Res. 29 (2014) 2036–2043, https://doi.org/10.1557/jmr.2014.131.
[9] P.J. Maziasz, G.M. Goodwin, D.J. Alexander, S. Viswanathan, Alloy Development and Processing of FeAl: an Overview, ASM International, 1996.
[10] V.K. Sikka, R.W. Swindeman, I.G. Wright, R.R. Judkins, R. Johnson, Fabrication of test tubes for coal ash corrosion testing, in: Oak Ridge National Lab (ORNL), 1999, pp. 1–7. Knoxville, TN.
[11] P. Kratochvíl, The history of the search and use of heat resistant Pyroferal© alloys based on FeAl, Intermetallics 16 (2008) 587–591, https://doi.org/10.1016/j.intermet.2008.01.008.
[12] J. Cebulski, Application of FeAl intermetallic phase matrix based alloys in the turbine components of a turbocharger, Metalurgija 54 (2015) 154–156.
[13] D.J. Gaydosh, M.V. Nathal, Influence of testing environment on the room temperature ductility of FeAl alloys, Scripta Metall. Mater. 24 (1990) 1281–1284, https://doi.org/10.1016/0956-716X(90)90342-E.
[14] D.G. Morris, M.A. Muñoz-Morris, J. Chao, Development of high strength, high ductility and high creep resistant iron aluminide, Intermetallics 12 (2004) 821–826, https://doi.org/10.1016/j.intermet.2004.02.032.
[15] A. Bahadur, Enhancement of high temperature strength and room temperature ductility of iron aluminides by alloying, Mater. Sci. Technol. 19 (2003) 1627–1634, https://doi.org/10.1179/026708303225008266.
[16] M. Palm, Concepts derived from phase diagram studies for the strengthening of Fe–Al-based alloys, Intermetallics 13 (2005) 1286–1295, https://doi.org/10.1016/j.intermet.2004.10.015.
[17] D.G. Morris, M.A. Muñoz-Morris, Development of creep-resistant iron aluminides, Mater. Sci. Eng. 462 (2007) 45–52, https://doi.org/10.1016/j.msea.2005.10.083.
[18] M. Palm, F. Stein, G. Dehm, Iron aluminides, Annu. Rev. Mater. Res. 49 (2019) 297–326, https://doi.org/10.1146/annurev-matsci-070218-125911.
[19] C.G. McKamey, J.A. Horton, The effect of molybdenum addition on properties of iron aluminides, Metall. Trans. A 20 (1989) 751–757, https://doi.org/10.1007/BF02667592.
[20] X. Li, P. Prokopčáková, M. Palm, Microstructure and mechanical properties of Fe–Al–Ti–B alloys with additions of Mo and W, Mater. Sci. Eng., A 611 (2014) 234–241, https://doi.org/10.1016/j.msea.2014.05.077.
[21] P. Morgand, P. Mouturat, G. Sainfort, Structure et proprietes mecaniques des alliages fer-aluminium, Acta Metall. 16 (1968) 867–875, https://doi.org/10.1016/0001-6160(68)90107-7.
[22] D.G. Morris, M.A. Muñoz-Morris, L.M. Requejo, Work hardening in Fe–Al alloys, Mater. Sci. Eng., A 460–461 (2007) 163–173, https://doi.org/10.1016/j.msea.2007.01.014.
[23] D. Risanti, J. Deges, L. Falat, S. Kobayashi, J. Konrad, M. Palm, B. Pöter, A. Schneider, C. Stallybrass, F. Stein, Dependence of the brittle-to-ductile transition temperature (BDTT) on the Al content of Fe–Al alloys, Intermetallics 13 (2005) 1337–1342, https://doi.org/10.1016/j.intermet.2005.02.007.
[24] H.P. Longworth, D.E. Mikkola, Effects of alloying additions of titanium, molybdenum, silicon, hafnium and tantalum on the microstructure of iron aluminides near Fe3Al, Mater. Sci. Eng. 96 (1987) 213–229, https://doi.org/10.1016/0025-5416(87)90555-6.
[25] Z. Sun, W. Yang, L. Shen, Y. Huang, B. Zhang, J. Yang, Neutron diffraction study on site occupation of substitutional elements at sub lattices in Fe3 Al intermetallics, Mater. Sci. Eng., A 258 (1998) 69–74, https://doi.org/10.1016/S0921-5093(98)00919-8.
[26] Y. Nishino, S. Asano, T. Ogawa, Phase stability and mechanical properties of Fe3Al with addition of transition elements, Mater. Sci. Eng., A 234–236 (1997) 271–274, https://doi.org/10.1016/S0921-5093(97)00191-3.
[27] R.T. Fortnum, D.E. Mikkola, Effects of molybdenum, titanium and silicon additions on the D03 - B2 transition temperature for alloys near Fe3Al, Mater. Sci. Eng. 91 (1987) 223–231, https://doi.org/10.1016/0025-5416(87)90301-6.
[28] R. Krein, M. Palm, M. Heilmaier, Characterization of microstructures, mechanical properties, and oxidation behavior of coherent A2 + L21 Fe-Al-Ti, J. Mater. Res. 24 (2009) 3412–3421, https://doi.org/10.1557/jmr.2009.0403.
[29] J.G. Kim, R.A. Buchanan, Pitting and crevice corrosion of iron aluminides in a mild acid-chloride solution, Corrosion 50 (1994) 658–668, https://doi.org/10.5006/1.3293541.
[30] A. Agarwal, M.J. Akhtar, R. Balasubramaniam, Effect of alloying on aqueous corrosion and mechanical behaviour of iron aluminide Fe3Al, J. Mater. Sci. 31 (1996) 5207–5213, https://doi.org/10.1007/bf00355926.
[31] M.A. Crimp, K. Vedula, Effect of boron on the tensile properties of B2 FeAl, Mater. Sci. Eng. 78 (1986) 193–200, https://doi.org/10.1016/0025-5416(86)90323-X.
[32] R. Krein, A. Schneider, G. Sauthoff, G. Frommeyer, Microstructure and mechanical properties of Fe3Al-based alloys with strengthening boride precipitates, Intermetallics 15 (2007) 1172–1182, https://doi.org/10.1016/j.intermet.2007.02.005.
[33] R.G. Bordeau, Development of Iron Aluminides, Air Force Wright Aeronautical Laboratories, Ohio, USA, 1987.

[34] ASTM E112, Test Methods for Determining Average Grain Size, ASTM International, n.d, doi:10.1520/E0112-13R21.
[35] DIN EN ISO 643:2020-06, Steels - Micrographic Determination of the Apparent Grain Size (ISO 643:2019, Corrected Version 2020-03); German Version EN ISO 643, Beuth Verlag GmbH, 2020, https://doi.org/10.31030/3141695 n.d.
[36] P.A. Stadelmann, Ems - a software package for electron diffraction analysis and HREM image simulation in materials science, Ultramicroscopy 21 (1987) 131–145, https://doi.org/10.1016/0304-3991(87)90080-5.
[37] C.A. Schneider, W.S. Rasband, K.W. Eliceiri, NIH Image to ImageJ: 25 years of image analysis, Nat. Methods 9 (2012) 671–675, https://doi.org/10.1038/nmeth.2089.
[38] DIN EN ISO 6507-1:2018-07, Metallic Materials - Vickers Hardness Test - Part 1: Test Method (ISO 6507-1:2018); German Version EN ISO 6507-1, Beuth Verlag GmbH, 2018, https://doi.org/10.31030/2778746 n.d.
[39] DIN EN ISO 6892-1:2020-06, Metallic Materials - Tensile Testing - Part 1: Method of Test at Room Temperature (ISO 6892-1:2019); German Version EN ISO 6892-1, Beuth Verlag GmbH, 2019, https://doi.org/10.31030/3132591 n.d.
[40] DIN EN ISO 6892-2:2018-09, Metallic Materials - Tensile Testing - Part 2: Method of Test at Elevated Temperature (ISO 6892-2:2018); German Version EN ISO 6892-2, Beuth Verlag GmbH, 2018, https://doi.org/10.31030/2864330 n.d.
[41] E. Popiel, M. Tuszyński, W. Zarek, T. Rendecki, Investigation of Fe3−xVxAl alloys with DO3 type structure by X-ray, magnetostatic and Mössbauer effect methods, Journal of the Less Common Metals 146 (1989) 127–135, https://doi.org/10.1016/0022-5088(89)90369-X.
[42] J. Kopeček, P. Kratochvíl, D. Rafaja, D. Plischke, Ordering in the sublattices of Fe3Al during the phase transformation B2↔D03, Intermetallics 7 (1999) 1367–1372, https://doi.org/10.1016/S0966-9795(99)00057-6.
[43] E.I. Gladyshevskii, T.F. Fedorov, YuB. Kuz'ma, R.V. Skolozdra, Isothermal section of the molybdenum-iron-boron system, Poroshkovaya Metall. 5 (1966) 305–309.
[44] A. Emdadi, S. Weiß, A comparative study of microstructure and hot deformability of a Fe–Al–Ta iron aluminide prepared via additive manufacturing and conventional casting, Crystals 12 (2022) 1709, https://doi.org/10.3390/cryst12121709.
[45] P.R. Mouton, Principles and Practices of Unbiased Stereology: an Introduction for Bioscientists, Johns Hopkins University Press, 2002, 0–8018–6797–5.
[46] F. Stein, M. Palm, Re-determination of transition temperatures in the Fe–Al system by differential thermal analysis, Int. J. Mater. Res. 98 (2007) 580–588, https://doi.org/10.3139/146.101512.
[47] M.G. Mendiratta, S.K. Ehlers, H.A. Lipsitt, D03-B2-α phase relations in Fe-Al-Ti alloys, Metall. Trans. A 18A (1987) 509–518.
[48] Ewelina Bernstock-Kopaczyńska, M. Jabłońska, Study of defects structure in Fe-Al alloys, Solid State Phenom. 203–204 (2013) 411–416. https://doi.org/10.4028/www.scientific.net/SSP.203-204.411.
[49] I. Baker, P. Nagpal, F. Liu, P.R. Munroe, The effect of grain size on the yield strength of FeAl and NiAl, Acta Metall. Mater. 39 (1991) 1637–1644, https://doi.org/10.1016/0956-7151(91)90251-U.
[50] W.D. Nix, H. Gao, Indentation size effects in crystalline materials: a law for strain gradient plasticity, J. Mech. Phys. Solid. 46 (1998) 411–425, https://doi.org/10.1016/S0022-5096(97)00086-0.
[51] E. Broitman, Indentation hardness measurements at macro-, micro-, and nanoscale: a critical overview, Tribol. Lett. 65 (2017) 23, https://doi.org/10.1007/s11249-016-0805-5.
[52] M.Z. Butt, P. Feltham, Solid-solution hardening, J. Mater. Sci. 28 (1993) 2557–2576, https://doi.org/10.1007/BF00356192.
[53] P. Feltham, Solid solution hardening of metal crystals, J. Phys. Appl. Phys. 1 (1968) 303–308, https://doi.org/10.1088/0022-3727/1/3/305.
[54] C.L. Fu, J. Zou, Site preference of ternary alloying additions in FeAl and NiAl by first-principles calculations, Acta Mater. 44 (1996) 1471–1478, https://doi.org/10.1016/1359-6454(95)00297-9.
[55] N.I. Medvedeva, YuN. Gornostyrev, D.L. Novikov, O.N. Mryasov, A.J. Freeman, Ternary site preference energies, size misfits and solid solution hardening in NiAl and FeAl, Acta Mater. 46 (1998) 3433–3442, https://doi.org/10.1016/S1359-6454(98)00042-1.
[56] J.H. Schneibel, E.D. Specht, W.A. Simpson, Solid solution strengthening in ternary B2 iron aluminides containing 3d transition elements, Intermetallics 4 (1996) 581–583, https://doi.org/10.1016/0966-9795(96)00041-6.
[57] M. Friák, J. Deges, R. Krein, G. Frommeyer, J. Neugebauer, Combined ab initio and experimental study of structural and elastic properties of Fe3Al-based ternaries, Intermetallics 18 (2010) 1310–1315, https://doi.org/10.1016/j.intermet.2010.02.025.
[58] A.J. Ardell, Precipitation hardening, Metall. Trans. A 16 (1985) 2131–2165, https://doi.org/10.1007/BF02670416.
[59] J.L. Jordan, S.C. Deevi, Vacancy formation and effects in FeAl, Intermetallics 11 (2003) 507–528, https://doi.org/10.1016/s0966-9795(03)00027-x.
[60] G. Hasemann, J.H. Schneibel, M. Krüger, E.P. George, Vacancy strengthening in Fe3Al iron aluminides, Intermetallics 54 (2014) 95–103, https://doi.org/10.1016/j.intermet.2014.05.013.
[61] S. Takeuchi, On the shear modulus parameter in the theory of solid-solution hardening, Scripta Metall. 2 (1968) 481–483, https://doi.org/10.1016/0036-9748(68)90177-4.
[62] R.J. Arsenault, The double-kink model for low-temperature deformation of B.C.C. metals and solid solutions, Acta Metall. 15 (1967) 501–511, https://doi.org/10.1016/0001-6160(67)90083-1.